

Vibration measurements of the gerbil eardrum under quasi-static pressure sweeps

Orhun Kose¹, W. Robert J. Funnell^{1,2,3}, Sam J. Daniel^{3,2}

J. Assoc. Res. Otolaryngol. 23(6): 739-750 (2022)

¹ Department of BioMedical Engineering, McGill University
3775, rue University, Montréal, QC, Canada H3A 2B4

² Department of Otolaryngology – Head and Neck Surgery, McGill University

³ Department of Pediatric Surgery, McGill University

E-mail addresses

orhun.kose@mail.mcgill.ca

robert.funnell@mcgill.ca

sam.j.daniel@mcgill.ca

This version of the article has been accepted for publication, after peer review, but is not the Version of Record and does not reflect post-acceptance improvements, or any corrections. The Version of Record is available online at <http://dx.doi.org/10.1007/s10162-022-00867-x>. Use of this Accepted Version is subject to the publisher's Accepted Manuscript terms of use (<https://www.springernature.com/gp/open-research/policies/accepted-manuscript-terms>).

ABSTRACT: Tympanometry provides an objective measurement of the status of the middle ear. During tympanometry, the ear-canal pressure is varied while the response of the ear to sound pressure is measured. The effects of the pressure on the mechanics of the middle ear are not well understood. This study is a continuation of our previous work in which the vibration response of the gerbil eardrum was measured in vivo under quasi-static pressure steps. In this study we delivered a continuous pressure sweep to the middle ear, and measured the vibration response at four locations for 6 gerbils. Vibrations were recorded using a single-point laser Doppler vibrometer and glass-coated reflective beads (diameter $\sim 40 \mu\text{m}$) at the umbo and on the mid-manubrium, posterior pars tensa and anterior pars tensa.

The vibration magnitudes were similar to those in the previous step-wise pressurization experiments. Most gerbils showed repeatability within less than 10 dB for consecutive cycles. As described in the previous study, as the frequency was increased at ambient pressure the vibration magnitude on the manubrium increased slightly to a broad peak (referred to as R1) then decreased until a small peak appeared (referred to as R2), followed by multiple peaks and troughs as the magnitude decreased further. The low-frequency vibration magnitude (at 1 kHz) decreased monotonically as the pressure became more negative except for a dip (about 500 Pa wide) that occurred between -700 and -1800 Pa. The lowest overall magnitude was recorded in the dip at mid-manubrium. The vibration magnitudes also decreased as the middle-ear pressure was made more positive and were larger than those at negative pressures. R1 was only visible at negative and small positive middle-ear pressures, while R2 was visible for both positive and negative pressures. R2 split into multiple branches after the middle-ear pressure became slightly positive. No magnitude dip was visible for positive middle-ear pressures.

The low-frequency vibration magnitudes at negative middle-ear pressures on the pars tensa were higher than those on the manubrium. R1 was not visible for large negative middle-ear pressures on the pars tensa. R2 appeared as a multi-peak feature on the pars tensa as well, and a higher-frequency branch on the posterior pars tensa appeared as a trough on the anterior pars tensa. The magnitude dip was not present on the pars tensa. The largest overall magnitude was recorded at the R2 peak on the posterior pars tensa.

The results of this study expand on the findings of the step-wise pressurization experiments and provide further insight into the evolution of the vibration response of the eardrum under quasi-static pressures.

KEYWORDS: middle ear, eardrum, vibration, laser Doppler vibrometry, static pressure, tympanometry

Introduction

Tympanometry provides a fast, objective and noninvasive measurement of the acoustic input admittance (and related quantities) of the external and middle ear in the presence of quasi-static pressures. In a tympanometer, a probe tip in the ear canal combines a speaker that introduces an acoustic signal, a microphone that records the sound pressure, and a pump that provides the quasi-static pressure sweeps. Clinical tympanometers typically use a low-frequency pure-tone acoustic signal (around 220 Hz), with pump speeds of somewhere between 2000 and 4000 Pa/s and pressures swept in one or both directions between 0 Pa and ± 2000 to 4000 Pa. In early work, Lidén et al. (1970) assessed tympanometry for detecting ossicular-chain disruption by collecting tympanograms of healthy subjects as well as those with conductive and sensorineural hearing loss. They noted several changes in the admittance due to abnormalities in the middle ear and suggested using 800 Hz as a probe-tone frequency for better sensitivity to abnormalities. Creten and Van Camp (1974) measured the admittance at 220 and 660 Hz at various pressurization rates, and found that the most accurate measure was achieved at very low rates (about 10 Pa/s). They also observed the different tympanogram shapes that occur at 660 Hz for normal ears. Their group later concluded that tracking the tympanometric peak pressure (TPP, the pressure at which the admittance magnitude is maximal) in a single sweep did not provide an accurate assessment of the middle-ear pressure. and suggested averaging the TPPs of sweeps in opposite directions (Decraemer et al., 1984). Therkildsen & Gaihede (2005) compared clinical tympanometers and found that higher pressurization rates did not affect TPP and attributed the observed small differences to differences in the direction of the static pressure sweep. More recently, wide-band tympanometry (admittance measurements over a range of frequencies instead of a single pure tone) has been used to identify patients with otosclerosis (Shahnaz et al., 2009), Eustachian tube dysfunction (Aithal et al., 2019) and Ménière's disease (Tanno et al., 2020), among other conditions.

There have been a number of studies that tried to provide more insight by studying the movements of the eardrum and ossicles under static pressures in human temporal bones. For example, Hüttenbrink(1988) performed extensive measurements for various conditions such as fixing the incudomalleolar joint and simulating the activation of the middle-ear muscles. He observed a complex 3D movement of the stapes during static pressurization of the middle ear. He also saw that the effect of muscle activation diminished as the static pressure on the eardrum became larger. Among other things, he concluded that 'gliding' movements in the incudomalleolar and incudostapedial joints are important; and that the middle-ear muscles are incapable of counterbalancing large static pressures but that the sheath of the tensor-tympani tendon provides a strong support. Dirckx and Decraemer (1991) recorded the shape of the eardrum while pressurizing the middle ear and concluded that the effects of positive and negative pressures were significantly different, and that the displacement of the malleus could not be modelled as undergoing a simple fixed-axis rotation at higher static pressures. Murakami et al. (1997) measured the vibration magnitudes of the umbo and the stapes with a tympanometer probe placed in the Eustachian tube to pressurize the middle ear. They saw that, for both positive and negative middle-ear pressures, the low-frequency vibration magnitudes decreased as the pressure was increased, and the frequency-response peaks shifted to higher frequencies. The displacements at higher frequencies increased as the pressure was increased. Gan et al. (2006) measured the effects of static pressure (and also of middle-ear fluid) and reported the displacements at the umbo and the stapes footplate. They found that increasing middle-ear pressures up to about +2 kPa reduced vibration magnitudes uniformly up to 1.5 kHz but had less effect for higher frequencies. For negative middle-ear pressures the umbo vibration magnitude decreased up to 1.5 kHz, but increased for higher frequencies. They also found that the cochlea had its greatest effect on the eardrum vibrations at 4 kHz. Homma et al. (2010) measured the effects of static pressures on bone conduction as well as air conduction, and found that the bone-conduction resonance also shifted to higher frequencies in the presence of static

pressures. Warnholtz et al. (2021) experimentally reduced the flexibility of the incudomalleal joint and measured the effects on sound transmission in the presence of static pressures. They concluded that the flexible joint allows better sound transmission in the presence of static pressures.

The effects of static pressures on admittance during tympanometry are not well understood, especially for infants (e.g., Myers et al., 2019), and animal models for the vibration response of the eardrum under tympanometry-like pressure sweeps can help provide insight by allowing for extensive in-vivo measurements that are not possible in humans. For example, von Unge et al. recorded in-vivo admittance (1991) and also post-mortem eardrum shape (1993) in gerbils using a series of pressure steps in the ear canal. They noted that disrupting the ossicular chain increased the admittance, while fixation reduced it. They also compared tympanograms at 220 and 660 Hz and described the emergence of multiple peaks at the higher frequency. Lee and Rosowski (2001) measured in-vivo vibration responses at the umbo and on the pars flaccida in gerbils with pressure steps in the middle ear. They confirmed the existence of the asymmetry observed in previous studies in gerbils, with the largest admittance changes occurring for negative middle-ear pressures. They also identified the existence of a multiple-peak tympanogram when the frequency was increased to 1 kHz or higher.

Other species have been used in addition to the gerbil. Ladak et al. (2004) measured the shape of the cat eardrum under middle-ear pressure steps. They observed that an immobilized malleus produced a more symmetric response to static pressures than a mobile malleus did. Wang et al. (2017) measured in-vivo chinchilla eardrum surface vibrations and recorded the changes due to the release of a built-up middle-ear pressure of around 1.4 kPa. They observed a magnitude increase in all quadrants of the eardrum up to 2 kHz, at which frequency all of the eardrum was vibrating in phase, with the largest amplitude in the posterior pars tensa. For higher frequencies, the vibration magnitude stayed approximately constant after the release of the middle-ear pressure. Salih et al. (2016) measured rabbit ears post mortem to quantify the non-linearity in the middle ear due to harmonic quasi-static pressures. They found that the harmonic distortion was less than 10% for pressures less than 0.1 kPa, but the distortion increased rapidly when the pressure was increased to 1 kPa. The harmonic distortion also increased as the frequency of the sinusoidal quasi-static pressure was increased.

In a recent paper (Kose et al., 2020) we presented in-vivo gerbil vibration responses on the pars tensa, pars flaccida and manubrium under a step-wise middle-ear pressurization protocol for 11 gerbils. We illustrated shifts of the vibration peaks, both in frequency and magnitude, and studied their behaviour throughout the pressurization cycle. We described the first two peaks that were present at similar frequencies on the pars tensa, pars flaccida and manubrium; these peaks changed rapidly for small pressures. After the second peak, other closely spaced peaks specific to each region were also discussed.

In order to be more relevant to tympanometry, the mechanics of the middle ear should be investigated with pressure sweeps rather than steps. Dirckx et al. (2006) measured the displacement of the rabbit umbo and stapes under quasi-static pressure sweeps in the ear canal. For pressurization rates lower than 1 kPa/s, they observed a significant change in the pressure at peak displacement. They also saw more hysteresis at the umbo than on the stapes. They suggested that lower pressurization rates could provide additional clinical information about friction in the ossicular chain.

Since the admittance of the middle ear is highly dependent on the vibration of the eardrum, measuring vibrations at multiple points on the eardrum is essential for understanding the admittance measured in tympanometry. In this study we present multi-point in-vivo gerbil eardrum vibration responses to pressure sweeps. The vibration magnitudes at two points on the manubrium and two points on the pars tensa are shown as functions of both frequency and middle-ear pressure, and the evolution of the magnitudes and frequencies of the peaks and troughs are explored in detail.

Materials & methods

This study has been reviewed by the Facility Animal Care Committee of the McGill University Health Centre Research Institute (protocol number 2011-5201). Male Mongolian gerbils (*Meriones unguiculatus*) were used, with body weights ranging from 50 to 100 g (Charles River Laboratories, St-Constant, QC). Of the eight most recent gerbils, we present results for the six who survived until the end of the experiment with good middle-ear pressurization. The anaesthetic regimen and the surgical process were almost identical to those that we used previously (Kose et al., 2020). Pentobarbital was administered intraperitoneally to ensure proper anaesthesia throughout the experiment (for induction, 35 mg/kg if the animal was less than 6 months old, or 50 mg/kg if 6 months old or older; for maintenance, half of the induction dose every 30 minutes or when needed). The xylazine doses that we used previously were omitted due to issues with slow induction and inconsistent levels of anaesthesia.

After an incision between the jaw and the shoulder, the bulla was exposed starting posteriorly and moving clockwise, and then the ear canal was removed down to the bony meatus. A small hole was created in the bulla to allow access to the middle ear for pressurization. A 3D-printed acoustic coupler was attached to the ear canal with dental cement to provide an enclosed access to the eardrum. A glass window, coated to be anti-reflective around the frequency of the measurement laser, allowed access for the laser beam to focus on the glass-coated beads on the eardrum. One bead was placed at the umbo, and another one roughly midway along the length of the manubrium. One bead was placed on the posterior pars tensa and one on the anterior pars tensa, at the level of the mid-manubrium and roughly halfway between the manubrium and the annulus (Kose et al. 2020, Figure 2). It should be noted that neither pars-tensa bead was placed to necessarily coincide with the highest vibration magnitude on the TM. These bead locations were the same as four of those reported in our previous paper. The pars flaccida was omitted in this study due to its large static displacements that quickly moved the bead out of focus, even for small pressures and the slow pressurization rate used here.

The pressurization system consisted of a peristaltic pump controlled by a microcontroller (Arduino Uno, SmartProjects, Strambino, Italy) which pressurized the middle ear via a small hole in the bulla. The system was the same as in Kose et al. (2020) except for the addition of a larger and adjustable buffer volume to provide a low pressurization rate during pressure sweeps. The static pressure was varied over a range of ± 2500 Pa. A full pressurization cycle included decreasing continuously from 0 Pa to -2500 Pa, increasing back to 0 Pa, increasing to $+2500$ Pa, and decreasing back to 0 Pa. The full pressure-cycle period was adjusted to be 210 ± 5 s, to match the length of one cycle of our previous step-wise pressurization protocol. As in our previous study, and in contrast to clinical tympanometric practice, the static pressure was applied in the middle-ear cavity and not in the ear canal. The pressure values here are reported in terms of the actual middle-ear pressure. The pressure sensor was accurate to within 12 Pa.

The vibrational velocities of beads on the manubrium and the pars tensa were measured using a laser Doppler vibrometer (LDV) (HLV-100, Polytec, Irvine, CA) and were recorded using Polytec's VibSoft software (Version 5.5). Both the sound pressure and the vibration velocity as functions of time throughout the pressurization cycle were stored in files with a unique identifier for each cycle, and a MATLAB script used their timestamps and identifiers to synchronize the measurements. A Python script (running on the same computer that managed the VibSoft output under Microsoft Windows 10) transmitted the target pressure extremes (± 2500 Pa) and the target pressurization speed to the Arduino microcontroller. After recording, the vibration velocities during each individual acoustic chirp (linear frequency sweep from 0.2 to 10 kHz) were integrated to obtain displacements and then converted to the frequency domain using a Fast Fourier Transform. The vibration displacement magnitudes (normalized by the sound pressure) were then plotted using a MATLAB script for all of the figures in the next section.

All measurements were recorded in a sound-isolation chamber where the animal and the microscope were placed on an anti-vibration pad on a table. The noise floor was recorded by focusing the vibrometer on the inside wall of the acoustic coupler at the beginning of each experiment. For the range of frequencies considered here, the measured magnitudes were at least an order of magnitude larger than the noise floor. The sound pressure level of the acoustic chirp was about 70 dB. No indications of middle-ear muscle reflexes were seen and the sound pressure was assumed to be well below the reflex activation threshold even for waking gerbils. The level of anesthesia was maintained such that the toe and eye twitch reflexes were absent.

At the beginning of each experiment, at least three consecutive pressurization cycles at the bead on the umbo were recorded. After three or more cycles at each of one or more of the other beads had been recorded, one or more final cycles were recorded at the umbo before sacrifice of the gerbil (pentobarbital overdose followed by pneumothorax). Figure 1 shows an example of the middle-ear pressure (black line) and the resulting umbo vibration magnitude (red line) at a single frequency (1.0 kHz) as a function of time throughout one pressurization cycle. The pressure signal consistently showed a slower linear loading phase (equivalent to a rate of 40 Pa/sec), and a faster nonlinear unloading phase (starting at a rate of ~ 70 Pa/sec and slowing to ~ 50 Pa/sec near 0 Pa). In order to display the vibration responses as functions of pressure in the spectrogram figures of the Results section, each chirp was matched to the static pressure at the corresponding time.

We chose the peaks based on peak width and height, as well as prioritizing continuity when the pressure was changed. Moreover, the locations of the peaks where they were harder to see were confirmed in other pressurization cycles at the same location for the same specimen. Details of the peak-finding criteria were described in Kose et al. (2020). Each identified peak in the vibration response coincided with a significant negative slope in the phase, while the troughs coincided with positive slopes.

The laser was manually aimed at the target bead at the beginning of each cycle, and re-aimed throughout the cycle when needed (e.g., when the bead moved outside the laser beam's diameter of ~ 35 μm). Especially near ambient pressure, the bead displacements were large in response to the quasi-static pressure change and the time required for the manual re-aiming sometimes resulted in an artifact due to a brief loss of the signal (as at $t \approx 7$ s and $t \approx 105$ s in Figure 1). In this particular measurement, the bead was also re-aimed near the highest positive pressure to ensure good signal strength (at $t \approx 160$ s). When higher pressurization rates were attempted, the manual re-aiming of the bead was no longer feasible.

As discussed in the previous paper, when the middle-ear pressure was made more negative, the low-frequency vibration magnitude decreased. At $t \approx 48$ s in the loading phase and $t \approx 78$ s in the unloading phase, there is a magnitude dip as the vibration magnitude becomes larger for more negative pressures. This phenomenon will be discussed further in the following sections.

Results

Inter-specimen variability

Figure 2 compares the inter-specimen variability of the unpressurized umbo responses of the 6 gerbils of this study with the responses of the 12 gerbils in Maftoon et al (2013) (blue shading) and the 11 gerbils in our previous paper (Kose et al., 2020) (red shading). The low-frequency magnitude (at 0.5 kHz) varied between 40 and 80 nm/Pa for our 6 gerbils while Maftoon et al. recorded between 30 and 100 nm/Pa and we previously recorded between 25 and 85 nm/Pa. The vibration magnitude increased as the frequency increased, up to a broad peak (referred to here as R1, as in our previous

paper) between 1.5 and 2.5 kHz, very similar in peak frequency and magnitude to what was shown in our previous paper. This peak coincides with a phase of around -90° . After the peak, the vibration magnitude decreased irregularly. The phase settled at around -180° above 6 kHz. The vibration magnitudes and the frequencies of the peaks, as well as the corresponding phase changes, were mostly within the ranges of those in our previous paper, with some small exceptions at higher frequencies.

For the following sections, gerbil G47 was chosen to show the vibration responses at various measurement locations because it was typical and it had the least noise and the fewest tracking artifacts.

Manubrial response

In order to compare the present pressure-sweep responses with the pressure-step responses from our previous paper, vibration frequency responses have been sampled at roughly 500-Pa intervals throughout the pressurization cycle. Figure 3 displays these sampled umbo vibration magnitudes (top panels) and phases (bottom panels) for the negative-pressure half-cycle (left panels) and the positive-pressure half-cycle (right panels), in the same format as for Figure 8 of our previous paper. At 0 Pa (solid black), the vibration magnitude increases from 35 nm/Pa at 0.5 kHz to a broad peak (R1, filled circular marker). This broad peak mostly coincides with a negative slope in phase, around -90° . After R1, the magnitude decreases until a hint of a peak (R2, as in the previous paper, filled square marker). R2 coincides with another negative phase slope, around -140° . For higher frequencies, the vibration magnitude decreases, more or less monotonically with multiple small peaks and troughs (including R3), to 5.6 nm/Pa at 10 kHz, where the phase becomes mostly flat at around -160° . All three peaks are difficult to discern in this pressure cycle but they were clearer in other cycles. The vibration magnitudes at 0.5 kHz decrease as the pressure is made more negative, reaching 6 nm/Pa at -500 Pa and 1.8 nm/Pa at -1000 Pa, while the slope between 0.5 kHz and R1 becomes flatter; beyond R1, the vibration magnitude decreases slightly before rising to R2. The phase is similar to what it was at 0 Pa, but the decrease to -90° occurs at a higher frequency as R2 shifts. The phase responses at the highest frequencies stay around -170° , with multiple small peaks and troughs corresponding to those seen in the magnitude. At -1500 Pa, the low-frequency vibration magnitude decreases to a very low value (around 0.09 nm/Pa) before rising slightly to R1; after R1 the vibration magnitude decreases again and then rises sharply to R2. The phase at this pressure kept on decreasing beyond 5 kHz, reaching -540° at 7 kHz (around R2) and -800° around 9 kHz. When the pressure is reduced to -2000 and -2500 Pa, the vibration magnitude stays more or less the same at 0.5 kHz but then, instead of decreasing sharply with increasing frequency, it increases gradually until R1 and then decreases slightly before rising to R2. The phase follows a pattern similar to the ones at -500 and -1000 Pa, but reaches -360° after R2. This decrease in the mid-frequency magnitudes, from about 0.5 kHz to 6 kHz, and for pressures between about -1000 Pa and -2000 Pa, was also observed in our previous paper, where it was described as a magnitude 'dip'.

At 0 Pa, R1 and R2 start as shallow peaks at 1.5 and 2.6 kHz with peak magnitudes of 100 nm/Pa and 54 nm/Pa, respectively. As the pressure becomes negative, both R1 and R2 rapidly shift to higher frequencies while their peak magnitudes decrease, reaching 2.8 and 4.5 kHz with peak magnitudes of 18 and 36 nm/Pa, respectively, at -500 Pa. As the pressure becomes more negative, R1 and R2 slowly shift further, reaching 3.0 and 6.8 kHz, respectively, at -1500 Pa. The R1 magnitude also shows a dip at -1500 Pa, decreasing to 0.12 nm/Pa. after which it recovers to 1.2 nm/Pa at -2500 Pa while shifting slightly to 3.1 kHz. The R2 peak magnitude, on the other hand, stays more or less constant around 9.2 nm/Pa at 7.8 kHz.

In the unloading phase of the negative-pressure half-cycle, the vibration magnitude is higher than or similar to that in the loading phase for pressures lower than -1000 Pa, especially at the magnitude dip

at -1500 Pa. As the pressure is increased from -2500 Pa to -1000 Pa, the low-frequency magnitudes between 0.5 kHz and R1, and those between R1 and R2, start to decrease. The magnitude between R1 and R2 is lowest around -1000 Pa during the unloading phase, similar to what is seen at -1500 Pa in the loading phase. The phase response is similar as well, reaching -820° around 9 kHz. When the magnitude dip is not present (i.e., on the PT in the negative pressure half-cycle and at all locations in the positive pressure half-cycle), the lowest low-frequency magnitude is usually at the extreme (± 2500 Pa) pressure. For pressures more positive than those of the dip, the vibration magnitudes for frequencies up to R2 recover rapidly but remain slightly less than in the loading phase.

The pattern is much simpler in the positive-pressure half-cycle. The low-frequency vibration magnitudes decrease monotonically when the pressure is increased, with very little change beyond $+2000$ Pa. R1 disappears for positive pressures in the loading phase while R2 shifts rapidly from 2.7 kHz at 0 Pa to 7.7 kHz at $+1000$ Pa, and then more slowly to 8.7 kHz at $+2500$ Pa. The phase response is also simple, starting around 0° and decreasing slowly until R2 where it reaches -90° . The phase stays around -180° for higher frequencies. When the pressure is reduced back to zero, the vibration magnitude increases to higher values than it had during the loading phase. R1 reappears as a shallow peak at 2.7 kHz and $+500$ Pa before shifting back to 1.4 kHz at 0 Pa, and R2 shifts back to an almost-buried peak at about 2.2 kHz at 0 Pa, both frequencies less than what was seen at the beginning of the negative-pressure half-cycle.

The overall trends here are very similar to what was seen with the step-wise pressurization protocol in our previous paper. For both negative-pressure and positive-pressure half-cycles, the low-frequency vibration magnitudes and the R1 and R2 frequencies and magnitudes in different pressurization cycles and in other gerbils were within the ranges of the ones in Kose et al. (2020). R3 was also observed in those earlier experiments but was not explicitly labelled.

To illustrate the continuous frequency-response evolution throughout the pressurization-sweep cycle, Figure 4 shows a spectrogram of the vibration magnitude at the umbo for G47 (the same data as shown in Figure 3). The horizontal axis is the quasi-static middle-ear pressure while the vertical axis is the frequency on a linear scale. Both R1 and R2 were traced where they were visible. Between 0 Pa and -300 Pa, both R1 (thick red line) and R2 (medium red line) are difficult to discern. After -400 Pa, R1 becomes faintly visible at about 2.7 kHz as a slight rightward convexity of the isomagnitude contours, and it then rises slowly to about 3.1 kHz at -2500 Pa. R2, on the other hand, appears as a sharp peak at 4 kHz by about -200 Pa and shifts rapidly to 7.8 kHz at -2500 Pa. Multiple higher-frequency peaks and troughs start to appear between 0 and -300 Pa, shifting rapidly to higher frequencies. The peak with the lowest frequency after R2 can be tracked throughout the cycle (thin red line), but peaks at higher frequencies shift beyond 10 kHz as the pressure becomes more negative.

When the pressure is decreased from zero to about -1100 Pa, the magnitude dip (described above) appears at about 5.9 kHz, near R2. The dip very rapidly shifts to 3.6 kHz at -1250 Pa, its range broadening until it extends from 0.5 to 5.1 kHz at -1400 Pa. The magnitude at the centre of this dip is about 0.2 nm/Pa. After being effectively buried in the dip, R1 reappears as a broad peak at about 3 kHz as the pressure drops to about -1700 Pa, reaching a magnitude of about 1 nm/Pa at -2500 Pa. The R2 magnitude also rapidly recovers after the dip, to 5.5 nm/Pa at -1300 Pa, and it continues to increase to 11 nm/Pa at 8.0 kHz by -2500 Pa. When the pressure is increased from -2500 Pa back to 0 Pa, the behaviour of the peaks is approximately the reverse of what happened in the loading phase, with a slight asymmetry. The magnitude dip occurs between about -1200 and -900 Pa in the unloading phase.

In the positive-pressure half-cycle, the vibration magnitudes are seen to change much less than in the negative-pressure half-cycle, as also seen in Figure 3. The R1 peak rapidly shifts to 2.8 kHz with a peak magnitude of 20 nm/Pa at $+350$ Pa (it is partially hidden due to the artifact between $+150$ and

+300 Pa) before disappearing for more positive pressures. The R2 frequency rapidly shifts from 0 Pa to +200 Pa, and then is seen with two separate branches; first one appears at 6.5 kHz at +700 Pa, and the second one appears at 7.7 kHz at +1200 Pa. Both shift further as the pressure reaches +2500 Pa, to 7.8 kHz and 8.8 kHz, respectively. After a sharp trough that follows a trajectory similar to that of the second branch of R2, another substantial peak (thin red line) also shifts to higher frequencies as the pressure is increased. In the unloading phase, the two branches of R2 converge at about 6.9 kHz at +1300 Pa, before shifting back to lower frequencies. R1 reappears at 4 kHz at +500 Pa, and shifts to lower frequencies when the pressure is reduced back to 0 Pa.

Figure 5 shows a collage of the spectrograms for all six gerbils. The features described for G47 are all also seen for the other gerbils, with some quantitative differences. All of the gerbils display a magnitude dip in the negative-pressure half-cycle, but there are some qualitative differences. For G49 the dip is divided by R1 (around 4 kHz), while the magnitude dip for G51 has 2 splits, being divided by R1 (around 3.5 kHz) and by a trough after R1 (around 4.2 kHz). The magnitude dip for G50 occurs for even higher frequencies than R2 (around 7 kHz in the loading phase). The magnitude dip in G49 occurs at a more negative pressure, and the vibration magnitude does not recover much at -2500 Pa. The splitting of R2 in the positive-pressure half-cycle is present in all of the gerbils, with some differences in the pressure and frequency at which they converge again.

Figure 6 shows another way of looking at the same data, with the vibration responses at several individual frequencies, from 0.5 to 10 kHz, shown as functions of the static pressure. Black lines indicate the loading phases while the red lines indicate the unloading phases. The green boxes show the locations of the R2 peaks in each half-cycle at each frequency. The vertical and horizontal dashed lines help locate the ambient pressure and the vibration magnitude at -2500 Pa, respectively. At 0.5 kHz the vibration magnitude is quite noisy. The largest magnitude occurs at 0 Pa and the smallest magnitudes occur at the ends of the sweeps (± 2500 Pa). As described for Figures 3 and 4, the magnitude decreases more in the negative-pressure half-cycle than in the positive-pressure half-cycle. From 1 to 5 kHz, magnitude dips are clearly visible in the negative-pressure half-cycle. From 1 kHz to about 2 kHz, the largest magnitude occurs at 0 Pa. The first three panels (0.5, 1 and 2 kHz) show curves analogous to clinical single-peak low-frequency tympanograms. At higher frequencies the magnitudes at -200 Pa and at +150 Pa become larger than the magnitude at 0 Pa. At 3 kHz (not shown), the largest magnitudes correspond to R2, at -250 Pa and at +250 Pa. At 4 and 5 kHz, the R2 peaks in the negative-pressure and positive-pressure half-cycles have similar magnitudes. The result is comparable to a W-shaped impedance tympanogram (or M-shaped admittance tympanogram) where admittance peaks occur at positive and negative ear-canal pressures, rather than there being a single peak at zero pressure (Vanhuysse et al., 1975). At 6 kHz, the magnitude dip is no longer visible, and the largest magnitude occurs at +600 Pa instead of in the negative-pressure half-cycle. At 8 and 10 kHz, there is a broad magnitude dip in the negative-pressure half-cycle between -600 Pa and -2000 Pa. The largest magnitude at 10 kHz corresponds to the higher-frequency peak (thin red line in Figure 4), at +2000 Pa.

The vibration responses at mid-manubrium were very similar to the ones at the umbo. For each gerbil, the frequencies of R2 and of the higher-frequency peaks were within 0.5 kHz of the ones at the umbo in the negative-pressure half-cycle, and within 0.8 kHz in the positive-pressure half-cycle. The low-frequency magnitude dip occurred at more negative pressures (from -1800 to -2200 Pa) than at the umbo.

Pars-tensa response

Figure 7 shows a spectrogram for the vibration response on the posterior pars tensa for the same gerbil as in Figure 4 (G47). Due to larger displacements of the pars tensa in response to the static pressure, more readjustments of the laser beam were necessary than for the umbo, resulting in more artifacts in

the vibration response (such as from 0 to -600 Pa, from -2200 to -2400 Pa, between the negative-pressure and positive-pressure half-cycles, etc.). As observed in our previous paper, the vibration responses on the pars tensa are similar overall to those at the umbo but with some key differences: the overall vibration magnitudes are larger; the magnitude dip in the negative-pressure half-cycle is absent for both pars-tensa points; and R1 disappears rapidly for large pressures, both negative and positive. The low-frequency magnitude on the posterior pars tensa (at 0.5 kHz) slowly decreases from 15 nm/Pa at -600 Pa to 1.8 nm/Pa as the pressure is reduced to -2500 Pa. Although hard to distinguish due to artifacts, R1 (thick red line) is an almost buried peak at 1.4 kHz (confirmed in other pressurization cycles at the same location in this ear) at 0 Pa, and shifts to 2.1 kHz at -400 Pa before disappearing for more negative pressures. The behaviour of R2 (medium red line) is similar to that seen at the umbo, shifting from 2.6 kHz at 0 Pa (peak magnitude 110 nm/Pa) to 3.8 kHz at -500 Pa (peak magnitude 100 nm/Pa), and then to 7.8 kHz at -2500 Pa (peak magnitude 39 nm/Pa). At about -300 Pa a cluster of peaks separates from R2, extending from 4.5 kHz to 6.8 kHz. (They are obscured due to the tracking artifact here, but they are confirmed by other cycles.) The peak with the lowest frequency within the cluster (denoted by the thin red line) shifts more slowly than the others, reaching 8.8 kHz at -2500 Pa with a magnitude of 40 nm/Pa. This peak has about the same frequency as the trough between R2 and the thin red line in Figure 4. As the pressure is increased back to zero, the low-frequency magnitude increases, reaching 61 nm/Pa at 0 Pa, and all of the peaks shift back to lower frequencies.

In the positive-pressure half-cycle, the low-frequency magnitude drops from 61 nm/Pa at 0 Pa to 3.3 nm/Pa at +2500 Pa. R1 shifts to 3.1 kHz at +300 Pa and is not visible when the pressure is increased further. R2 and the cluster of peaks quickly diverge and shift to higher frequencies until +450 Pa where R2 reaches 4.1 kHz with a peak magnitude of 30 nm/Pa. R2 reaches 7.1 kHz at +2500 Pa with a peak magnitude of 1.5 nm/Pa, while the second branch reaches 8.9 kHz with a peak magnitude of 30 nm/Pa. The highest-frequency peak of the cluster reaches 9.9 kHz at +2000 Pa. A minimum lies between the two lowest-frequency branches of R2. This minimum reaches 7.3 kHz at +2500 Pa, and stays about 0.1 to 0.3 kHz higher in frequency than the first branch of R2. When the pressure is reduced back to 0 Pa, the low-frequency vibration magnitude increases back to 90 nm/Pa, while R1 becomes visible at +500 Pa around 3.5 kHz and shifts back to 1 kHz at 0 Pa. R2 shifts back to 4.4 kHz at +300 Pa, where it joins the cluster of peaks and shifts back to 3.6 kHz with a peak magnitude of 181 nm/Pa. The trough between the clusters disappears at about 6.3 kHz at +700 Pa.

The anterior pars-tensa response for the same gerbil (Figure 8) was generally similar to that of the posterior pars tensa. The R2 frequency in the negative-pressure half-cycle was within 0.5 kHz of that for the posterior pars tensa (as well as those of the umbo and mid-manubrium). The sharp peak that diverged from the cluster of peaks (R3) on the posterior pars tensa in the negative-pressure half-cycle was replaced by a sharp minimum on the anterior pars tensa. On the other hand, the sharp trough that followed the lowest-frequency branch of R2 on the posterior pars tensa in the positive-pressure half-cycle was replaced by a sharp peak on the anterior pars tensa. The 500-to-1000-Hz vibration magnitudes for the two pars-tensa points were similar to each other throughout the pressure cycle, with the exception of pressures more negative than -1500 Pa, where the vibration magnitudes on the anterior pars tensa were generally larger than those on the posterior pars tensa. The pars-tensa magnitudes were similar to that at the umbo at 0 Pa, about 100 nm/Pa. As the static pressure was decreased to -2500 Pa, the umbo low-frequency magnitude decreased to less than 1 nm/Pa while the posterior and anterior pars-tensa magnitudes stayed above 3.5 nm/Pa and 2 nm/Pa, respectively. In the positive-pressure half-cycle, the ratio of umbo to low-frequency magnitude at both pars tensa points remained at about unity for all pressure levels.

In other gerbils the pars-tensa responses were very similar to what is described here for G47 except that in G46 and G52 even the cluster peak with the lowest frequency shifted rapidly to higher frequencies

on both the anterior and posterior pars tensa as the pressure was made more negative; and in some G50 and G52 the sharp minimum on the anterior pars tensa (which appeared in the place of the sharp peak in the posterior pars tensa) also split for pressures lower than about -1500 Pa.

Discussion

In this paper we have expanded upon the findings of Kose et al. (2020), by observing the gradual changes in the vibration response under quasi-static pressure sweeps. The vibration magnitudes and peak frequencies found here with the sweeps were the same as those identified in the previous paper using steps, within the range of inter-specimen variability. This is consistent with the idea that the pressure sweep was slow enough to be similar to the series of steps in terms of viscoelastic effects (after the initial transient of the step subsides). With the sweeps, the rapid shifts of the peaks for small pressure changes (smaller than the 500-Pa steps of the previous paper) could be studied, as could the shifts of the numerous high-frequency features.

The pressurization rate was non-uniform but consistently so. The effect of this non-uniform rate was presumably small since the greatest rate change occurred at the beginnings of the unloading phases, near the extreme pressure values where the changes in displacement were smallest.

For both the manubrial and pars-tensa points, the dependence of the vibration magnitude on static pressure resembled a single-peak tympanogram at low frequencies (Figure 6, 0.5 kHz). However, as the frequency increased, more complex shapes were caused by the local peaks and troughs and by the dip at about -1500 Pa. Lee and Rosowski (2001) showed complex displacement curves in gerbils at frequencies as low as 4 kHz, which is in line with our umbo response. The separate peaks in the negative-pressure and positive-pressure half-cycles (our Figure 6, at 4 and 5 kHz) coincide with our R2 peaks, and as the frequency is increased further they create more complex displacement curves.

Lee and Rosowski (2001) observed magnitude dips at negative middle-ear pressures between 1 kHz and 4 or 6 kHz, while in our experiments the dip was visible from 0.5 kHz up to 5 or 6 kHz. Their dip was visible around -2000 Pa when they swept the pressures from negative to positive, and around -1000 Pa when they swept from positive to negative. In our results the effect of the sweep direction was smaller, with the dip occurring around -1400 Pa for negative-to-positive sweeps and around -1100 Pa for positive-to-negative sweeps. They attributed the differences between the directions to viscoelastic effects in the middle ear. They also suggested that the behaviour for negative middle-ear pressures could be affected by the pars flaccida sticking to the head of the malleus. Feizollah (2019) observed a phenomenon that might be relevant to the magnitude dip: under quasi-static pressure sweeps, the displacements of the incudostapedial joint increased as the ear-canal pressure increased up to $+1000$ Pa and then decreased for more extreme pressures.

As described in our previous paper, the low-frequency peak (designated as R1) occurs at all of the measured locations, but with differences in the range of pressures where it is visible: on the manubrium it disappears at large positive middle-ear pressures but is still visible at negative pressures, while on the pars tensa it disappears at both positive and negative large pressures. It is not clear whether this might be related to the conclusion by Homma et al. (2010), based on a combination of experimental measurements and modelling, that for positive ear-canal pressures (or negative middle-ear pressures) the stiffening of the eardrum may be greater than that of the ligaments that act on the malleus, while for negative ear-canal pressures (or positive middle-ear pressures) their degrees of stiffening may be similar.

The largest peak (designated as R2) was visible on both the manubrium and the pars tensa. It seems to be a superposition of multiple resonances at small pressures, since at higher pressures it appears to split

into multiple peaks on the pars tensa. The lowest-frequency branch of R2 on the posterior pars tensa appears to correspond in frequency to a trough on the anterior pars tensa. This is consistent with previous studies that have shown peaks at high frequencies that are local to specific regions of the pars tensa and are out of phase with vibrations in other regions (e.g., Decraemer et al., 1997 in cat; as cited by Fay et al., 2006; Cheng et al., 2013 in human; Maftoon et al., 2013 in gerbil).

The observations of the gradual changes of vibration magnitudes in response to slow pressure sweeps provide insight into the mechanoacoustical response of the middle ear under tympanometric pressures. In particular, the fine resolution for both the static pressure and the frequency allows a detailed look at the evolution of the tympanograms from single-peak V-shaped curves to more complex shapes as various parts of the middle ear start resonating at different frequencies. The mechanisms underlying the evolution of the peaks and the presence of the magnitude dip could be explored with a computational model validated using the present experimental data. To be more closely related to tympanometry, however, the effects of pressurization rates closer to those of clinical tympanometers should be investigated experimentally. Measurements at faster pressurization rates could be achieved by an automated bead-tracking system. In addition, faster bead tracking could allow measurements in regions with faster displacement changes, such as the pars flaccida. Simultaneous pressurized shape and vibration measurements of the eardrum could be invaluable in understanding the mechanics of the middle ear during tympanometry.

Acknowledgements

The authors would like to thank Dr. Aurore Dodelet-Devillers of the McGill University Health Centre Research Institute Vivarium, for her help with the handling of the animals, anaesthesia, and surgical procedures, and the rest of the Vivarium staff for their help in maintaining and advising on the health and comfort of the animals. We also thank Dr. Ross Wagner for his help in the development of the acoustic coupler and the experimental setup, and Mr. Sajjad Feizollah for his help with the surgical procedure and the development of the pressure control for the sweep. This work was supported in part by the Canadian Institutes of Health Research, the Natural Sciences and Engineering Research Council (Canada), the Fonds de recherche en santé du Québec, the Montréal Children's Hospital Research Institute, and the McGill University Health Centre Research Institute.

Conflict-of-interest disclosure statement

The authors declare that they have no conflicts of interest

References

- Aithal, S., Aithal, V., Kei, J., Anderson, S., & Liebenberg, S. (2019). Eustachian tube dysfunction and wideband absorbance measurements at tympanometric peak pressure and 0 daPa. *J. Am. Acad. Audiol.*, *30*(9), 781–791.
- Cheng, J. T., Hamade, M., Merchant, S. N., Rosowski, J. J., Harrington, E., & Furlong, C. (2013). Wave motion on the surface of the human tympanic membrane: Holographic measurement and modeling analysis. *J. Acoust. Soc. Am.*, *133*(2), 918–937.
- Creten, W. L., & Van Camp, K. J. (1974). Transient and quasi-static tympanometry. *Scand. Audiol.*, *3*(1), 39–42.
- Decraemer, W. F., Creten, W. L., & Van Camp, K. J. (1984). Tympanometric middle-ear pressure determination with two-component admittance meters. *Scand. Audiol.*, *13*(3), 165–172.
- Decraemer, W. F., Khanna, S. M., & Funnell, W. R. J. (1997). Vibrations of the cat tympanic membrane measured with high spatial resolution. Presented at the 20th Midwinter Res. Mtg. Assoc. Res. Otolaryngol., St. Petersburg Beach, FL.
- Dirckx, J. J. J., Buytaert, J. A. N., & Decraemer, W. F. (2006). Quasi-static transfer function of the rabbit middle ear, measured with a heterodyne interferometer with high-resolution position decoder. *J. Assoc. Res. Otolaryngol.*, *7*(4), 339–351.
- Dirckx, J. J. J., & Decraemer, W. F. (1991). Human tympanic membrane deformation under static pressure. *Hear. Res.*, *51*(1), 93–105.
- Fay, J. P., Puria, S., & Steele, C. R. (2006). The discordant eardrum. *Proc. Natl. Acad. Sci.*, *103*(52), 19743–19748.
- Feizollah, S. (2019). *Microstructure and displacements of the gerbil incudostapedial joint under static pressures* (M.Eng. thesis). Montréal, Canada: McGill University.
- Gan, R. Z., Dai, C., & Wood, M. W. (2006). Laser interferometry measurements of middle ear fluid and pressure effects on sound transmission. *J. Acoust. Soc. Am.*, *120*(6), 3799–3810.
- Homma, K., Shimizu, Y., Kim, N., Du, Y., & Puria, S. (2010). Effects of ear-canal pressurization on middle-ear bone- and air-conduction responses. *Hear. Res.*, *263*(1), 204–215.
- Hüttenbrink, K. B. (1988). The mechanics of the middle-ear at static air pressures: The role of the ossicular joints, the function of the middle-ear muscles and the behaviour of stapedial prostheses. *Acta Otolaryngol. (Stockh.)*, *105*(sup451), 1–35.
- Kose, O., Funnell, W. R. J., & Daniel, S. J. (2020). Vibration measurements of the gerbil eardrum under quasi-static pressure steps. *J. Assoc. Res. Otolaryngol.*, *21*(4), 287–302.
- Ladak, H. M., Decraemer, W. F., Dirckx, J. J. J., & Funnell, W. R. J. (2004). Response of the cat eardrum to static pressures: mobile versus immobile malleus. *J. Acoust. Soc. Am.*, *116*(5), 3008–3021.
- Lee, C.-Y., & Rosowski, J. J. (2001). Effects of middle-ear static pressure on pars tensa and pars flaccida of gerbil ears. *Hear. Res.*, *153*(1), 146–163.
- Lidén, G., Peterson, J. L., & Björkman, G. (1970). Tympanometry. *Arch. Otolaryngol.*, *92*(3), 248–257.
- Maftoon, N., Funnell, W. R. J., Daniel, S. J., & Decraemer, W. F. (2013). Experimental study of vibrations of gerbil tympanic membrane with closed middle ear cavity. *J. Assoc. Res. Otolaryngol.*, *14*(4), 467–481.
- Murakami, S., Gyo, K., & Goode, R. L. (1997). Effect of middle ear pressure change on middle ear mechanics. *Acta Otolaryngol. (Stockh.)*, *117*(3), 390–395.
- Myers, J., Kei, J., Aithal, S., Aithal, V., Carlie, D., Asaduzzaman, K., Manuel, A., Joseph, A., & Malicka, A. N. (2019). Diagnosing conductive dysfunction in infants using wideband acoustic immittance: Validation and development of predictive models. *J. Speech Lang. Hear. Res.*, *62*(9), 3607–3619.

- Salih, W. H. M., Soons, J. A. M., & Dirckx, J. J. J. (2016). 3D displacement of the middle ear ossicles in the quasi-static pressure regime using new X-ray stereoscopy technique. *Hear. Res.*, *340*, 60–68.
- Shahnaz, N., Longridge, N., & Bell, D. (2009). Wideband energy reflectance patterns in preoperative and post-operative otosclerotic ears. *Int. J. Audiol.*, *48*(5), 240–247.
- Tanno, G. A. Y., Santos, M. A. de O., Sanches, M. T. D., Durante, A. S., Almeida, K. de, Gameiro, M. S., Roque, N. M. C. de F., & Sousa Neto, O. M. de. (2020). Analysis of wideband tympanometry in Ménière's disease. *Braz. J. Otorhinolaryngol.*, *88*(2), 194–203
- Therkildsen, A. G., & Gaihede, M. (2005). Accuracy of tympanometric middle ear pressure determination: The role of direction and rate of pressure change with a fast, modern tympanometer. *Otol. Neurotol.*, *26*(2), 252–256.
- von Unge, M., Bagger-Sjöbäck, D., & Borg, E. (1991). Mechanoacoustic properties of the tympanic membrane: a study on isolated Mongolian gerbil temporal bones. *Am. J. Otol.*, *12*(6), 407–419.
- von Unge, M., Decraemer, W. F., Bagger-Sjöbäck, D., & Dirckx, J. J. J. (1993). Displacement of the gerbil tympanic membrane under static pressure variations measured with a real-time differential moire interferometer. *Hear. Res.*, *70*(2), 229–242.
- Vanhuyse, V. J., Creten, W. L., & Van Camp, K. J. (1975). On the w-notching of tympanograms. *Scand. Audiol.*, *4*(1), 45–50.
- Wang, B., Ghanta, P., Vinnikova, S., Bao, S., Liang, J., Lu, H., & Wang, S. (2017). Wrinkling of tympanic membrane under unbalanced pressure. *J. Appl. Mech.*, *84*(4), 041002.
- Warnholtz, B., Schär, M., Sackmann, B., Lauxmann, M., Chatzimichalis, M., Prochazka, L., Dobrev, I., Huber, A. M., & Sim, J. H. (2021). Contribution of the flexible incudo-malleal joint to middle-ear sound transmission under static pressure loads. *Hear. Res.*, 108272.

Figures

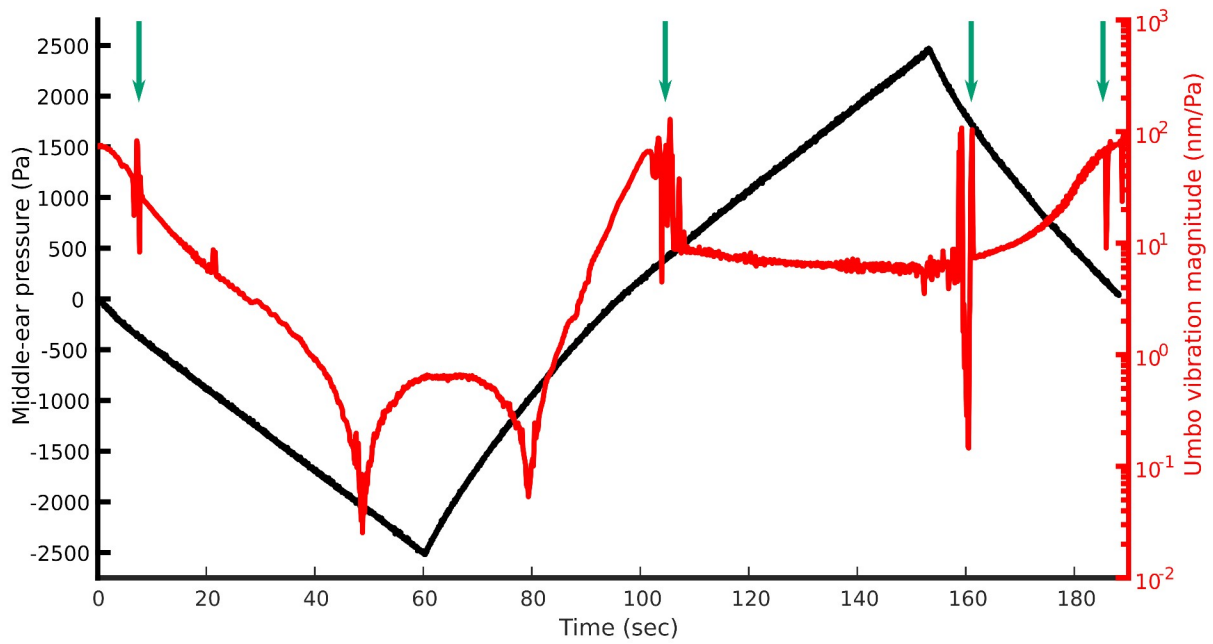


Figure 1: Middle-ear pressure (black) and corresponding vibration response (red) at 1.0 kHz for gerbil G47 at the umbo, for a single cycle.

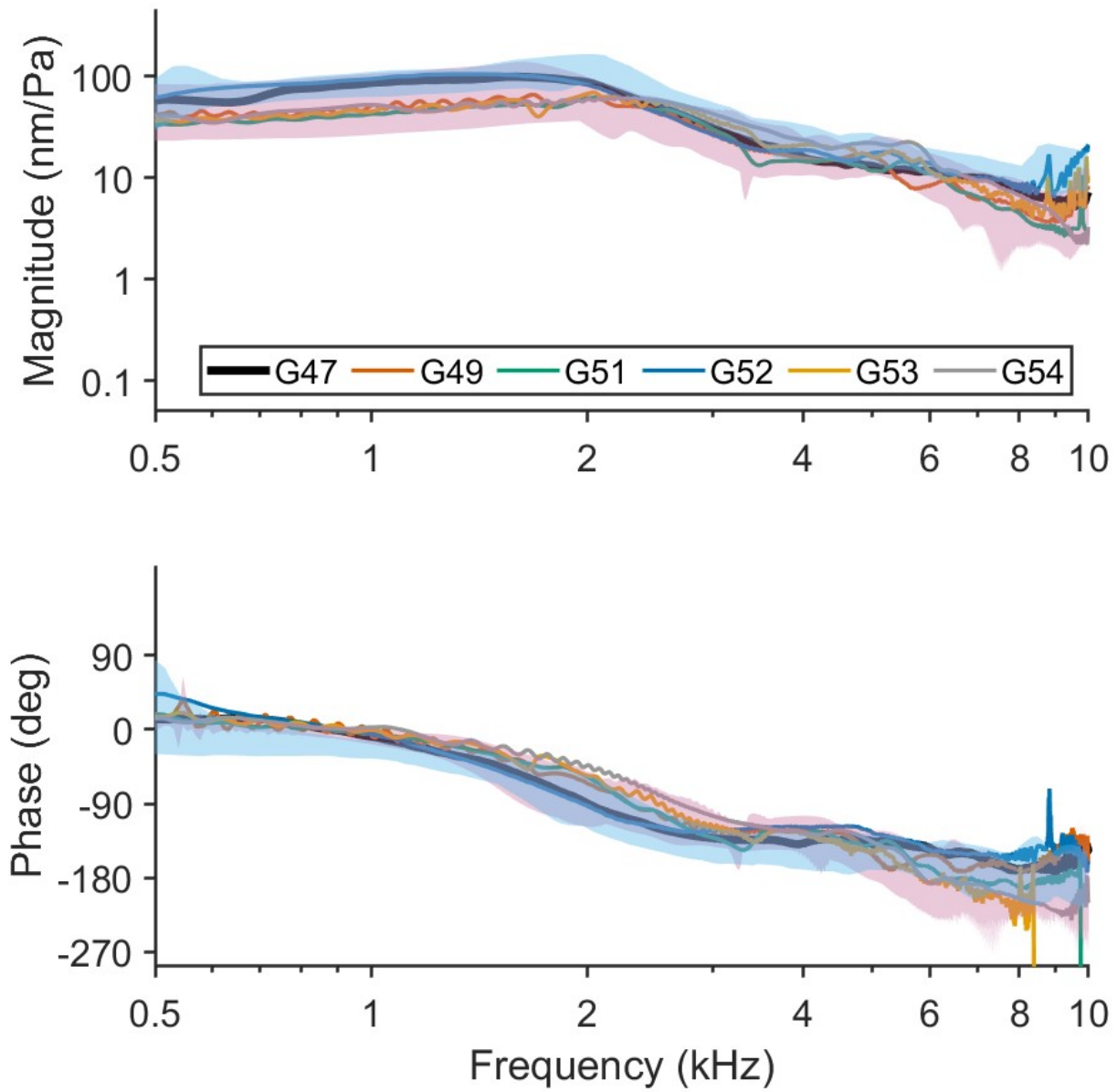


Figure 2: Unpressurized vibration magnitude (top) and phase (bottom) at the umbo for all 6 gerbils. Red and blue shaded areas are the vibration magnitude and phase ranges for the 11 gerbils reported in Kose et al. (2020) and the 12 gerbils reported in Maftoon et al. (2013), respectively.

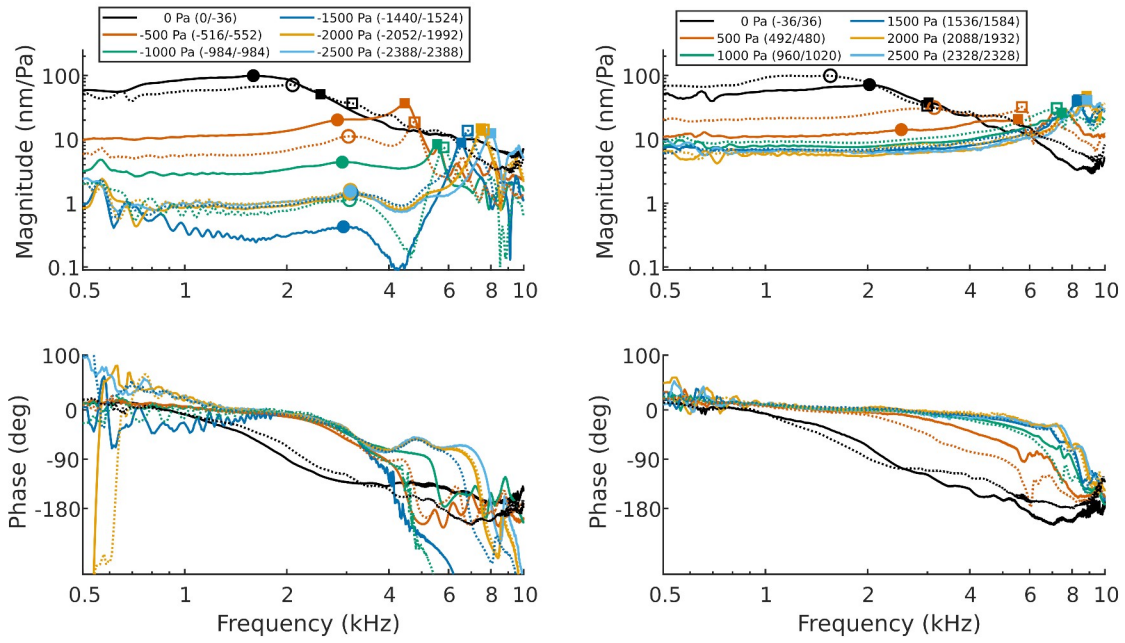


Figure 3: Vibration magnitude (top panels) and phase (bottom panels) of G47 at the umbo for negative-pressure half-cycle (left panels) and positive-pressure half-cycle (right panels). Solid curves = loading phase, dashed = unloading phase. Circles (R1) and squares (R2) show the locations of the resonances in the loading (filled symbols) and unloading (empty symbols) phases. (Actual pressure values are given in parentheses for both loading and unloading phases.)

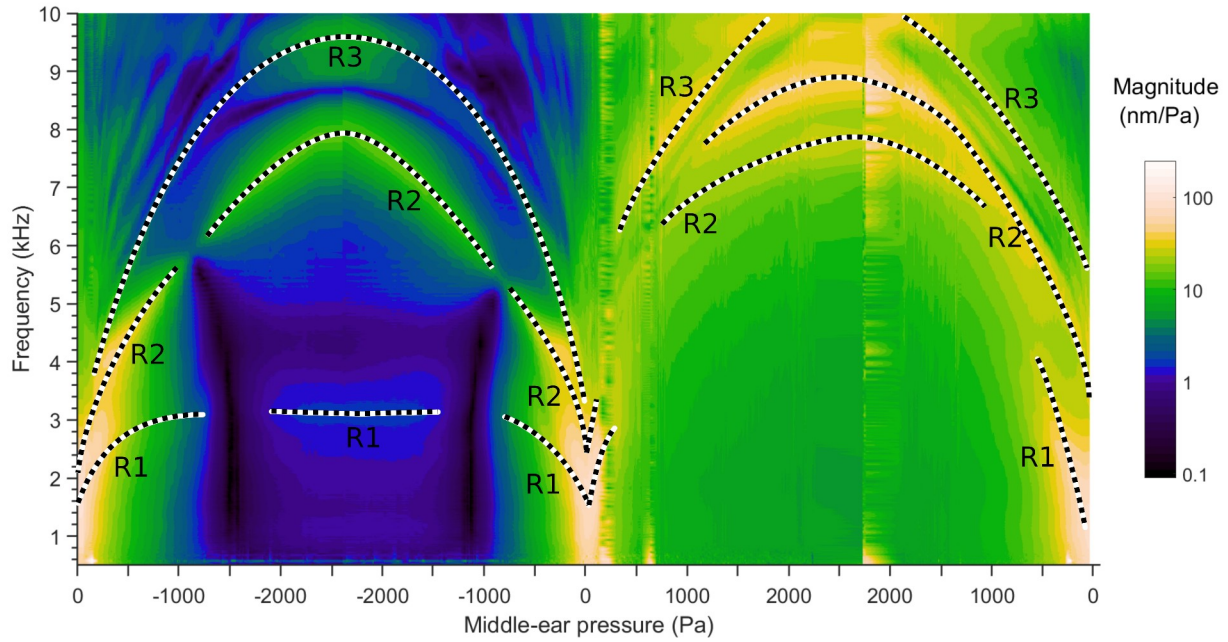


Figure 4: Vibration response of G47 at the umbo over the pressurization cycle as a spectrogram. The vertical axis shows the frequency on a linear scale. The trajectories of R1, R2, R3 and their branches are highlighted.

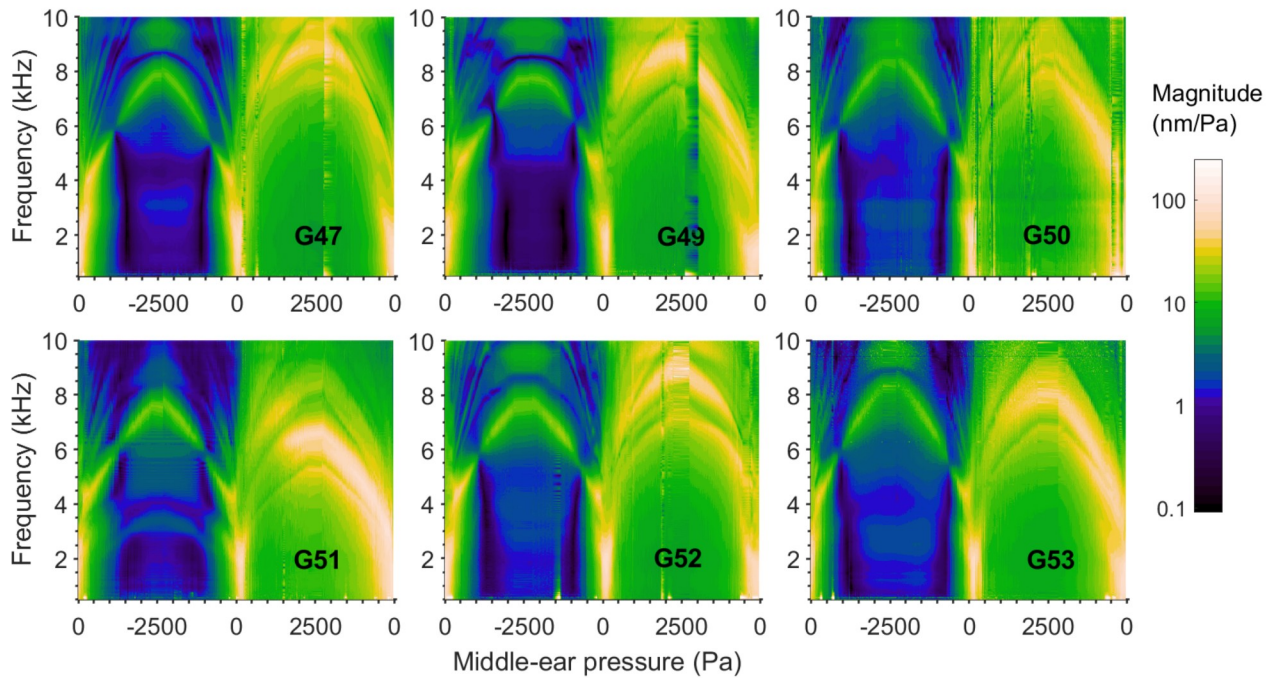


Figure 5: Vibration response of all 6 gerbils at the umbo over the pressurization cycle as a spectrogram. The vertical axis shows the frequency on a linear scale.

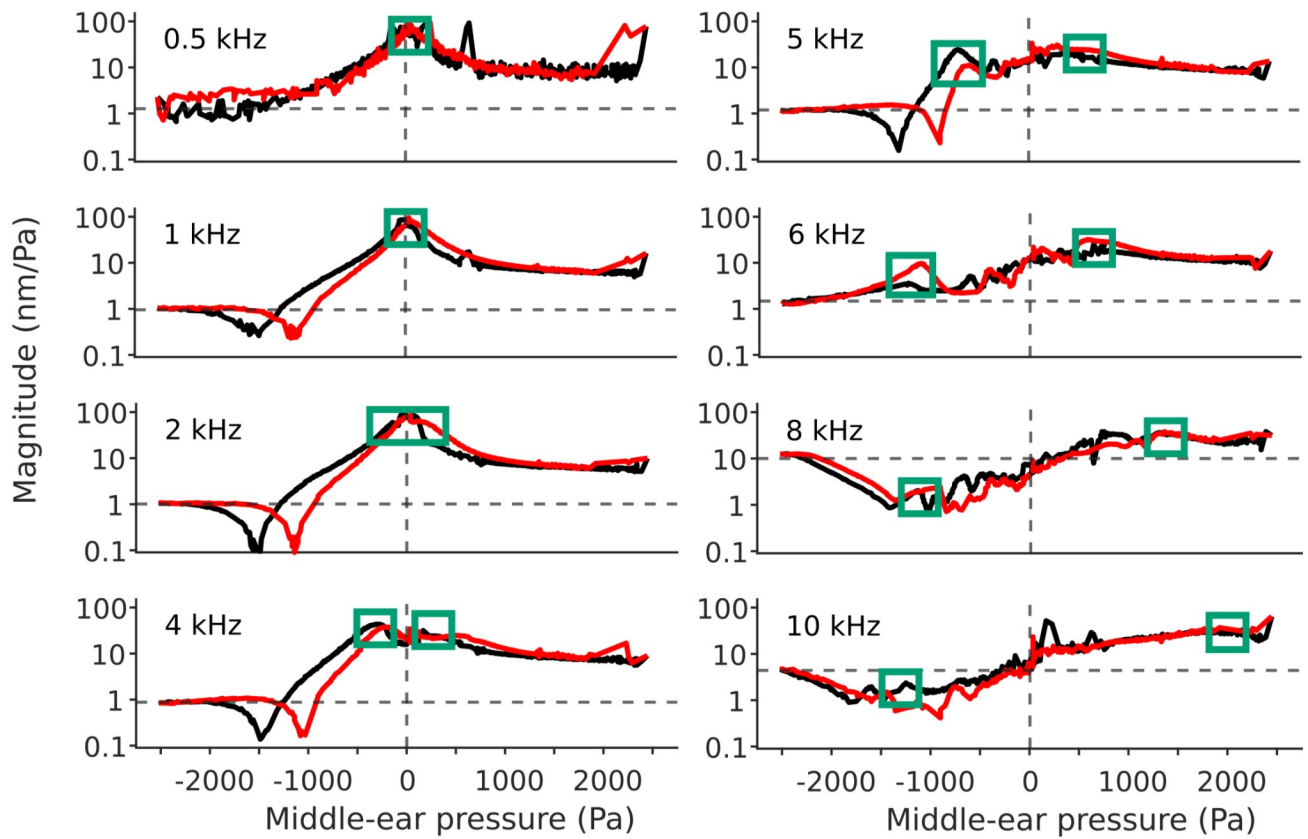


Figure 6: Vibration responses of G47 at the umbo as functions of the middle-ear pressure, at several frequencies. Green boxes show the locations of the highest magnitude (at 0.5, 1 and 2 kHz) or of R2 (for frequencies > 2 kHz).

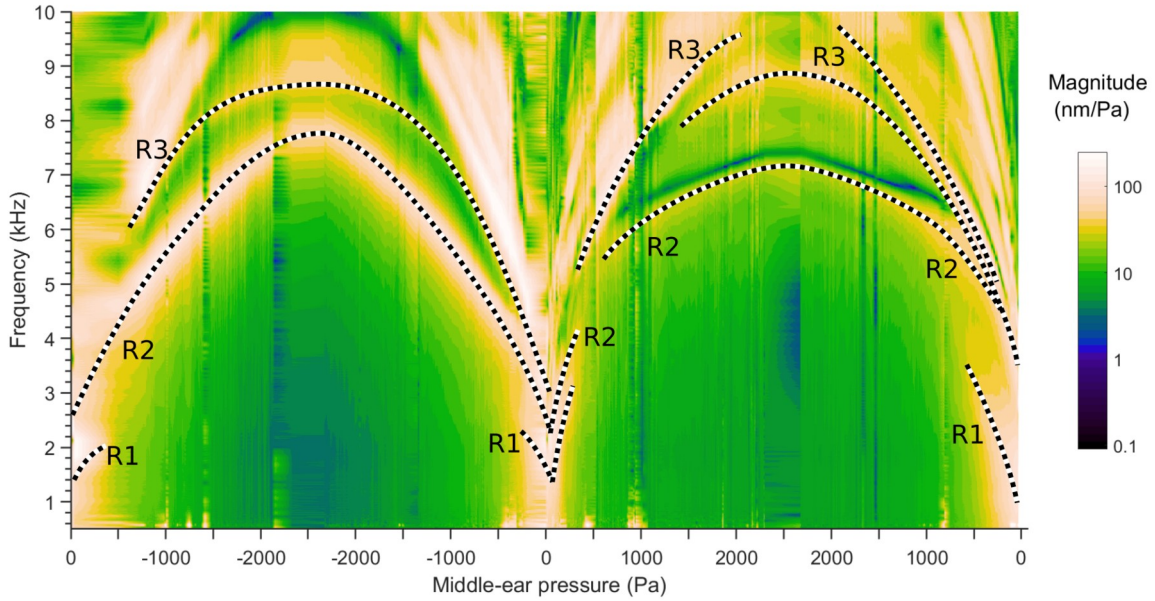


Figure 7: Vibration response of G47 on the posterior pars tensa over the pressurization cycle as a spectrogram. The vertical axis shows the frequency on a linear scale. The trajectories of R1, R2, R3 and their branches are highlighted.

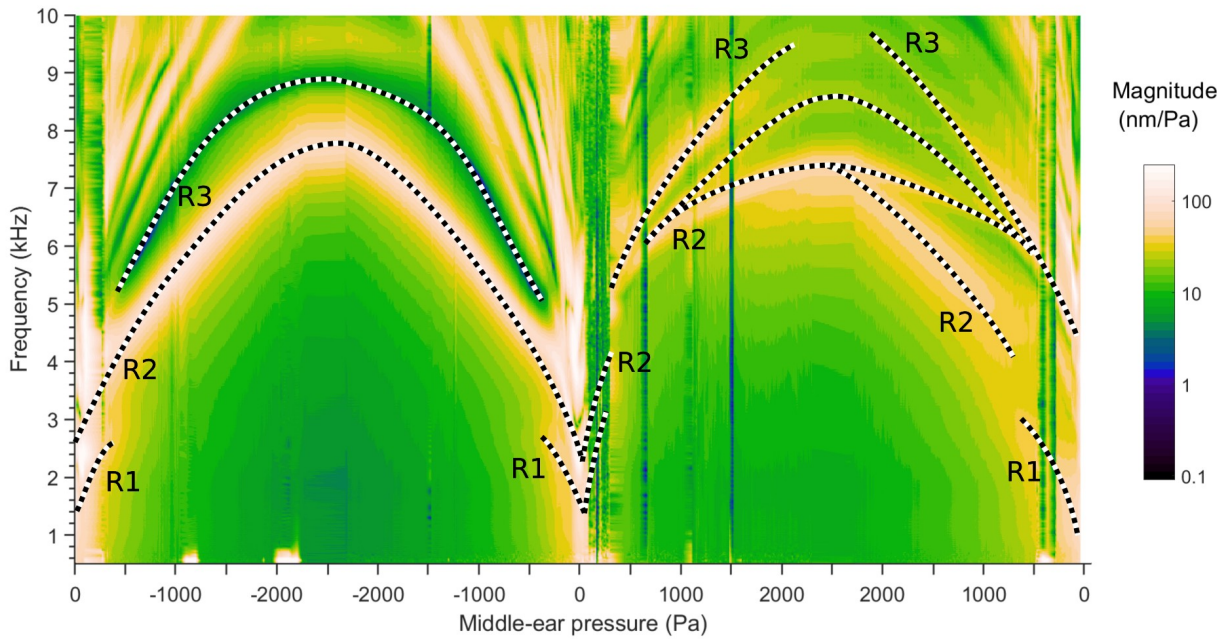


Figure 8: Vibration response of G47 on the anterior pars tensa over the pressurization cycle as a spectrogram. The vertical axis shows the frequency on a linear scale. The trajectories of R1, R2, R3 and their branches are highlighted.